Photoinduced acceleration of Fe^{3+}/Fe^{2+} cycle in heterogeneous FeNi-MOFs to boost peroxodisulfate activation for organic pollutant degradation

Dengke Wang [1], Mengjuan Suo [1], Shiqin Lai, Lanqing Deng, Jiayi Liu, Jun Yang, Siqi Chen, Mei-Feng Wu, Jian-Ping Zou [*]

Key Laboratory of Jiangxi Province for Persistent Pollutants Control and Resources Recycle, Nanchang Hangkong University, Nanchang 330063, PR China

ARTICLE INFO

ABSTRACT

The sluggish regeneration rate of Fe^{2+} in Fe-based heterogeneous catalysts restricts their wider application in persulfate-based advanced oxidation process (PS-AOPs). To conquer such challenge, Fe-embedded Ni-based metal-organic frameworks (FeNi-MOFs) with heteroatomic metal nodes were prepared and employed for persulfate activation to construct highly efficient PS-AOPs. Spectral analyses and density functional theory (DFT) calculations elucidated that the ligand-to-metal charge transfer and polarization of adjacent Ni centers endowed accelerated Fe^{3+}/Fe^{2+} redox cycle in the resultant FeNi-MOFs under light irradiation and thus promoted the Fe^{2+} recovery with Fe^{3+}/Fe^{2+} cycling efficiency > 58%. Consequently, the FeNi-MOFs delivered remarkable performance in peroxodisulfate activation and higher specific activity than that of the control Ni-MOFs/Fe^{3+} and state-of-the-art catalysts reported to date. This study provides new avenue of the accelerating Fe^{3+}/Fe^{2+} circulation in entirely heterogeneous systems for persulfate activation and also highlights the great potential of MOFs in design of high-performance Fe-based catalysts for PS-AOPs.

1. Introduction

Persulfate-based advanced oxidation process (PS-AOPs) represents an important water treatment technology for the remediation of recalcitrant organic contaminants [1]. In principle, PS-AOPs involves the activation of persulfate to generate various reactive oxygen species, which largely determine the catalytic performance of the entire process [2]. In recent decades, many advanced catalysts based on Co [3], Ag [4], Fe [5] and Mn [6] components have been designed to promote the persulfate activation and decontamination efficacy. Heterogeneous Fe-containing materials have been widely studied as applicable prototype due to their environmentally-friendly and size-dependant electronic properties for charge transformation [7]. However, persulfate activation over most Fe-containing catalysts is usually restricted by the sluggish kinetics of the Fe^{3+}/Fe^{2+} redox cycle. Besides, leaching of Fe components occurs in most developed systems, which ultimately deteriorates the efficiency of persulfate activation. Although strategies like introducing homogeneous organic reductants and/or heterogeneous co-catalysts have been reported to accelerate the Fe^{2+} recovery [8,9], the performance of these systems remains far from satisfactory. In

addition to being limited by their addition amount, homogeneous organic reductants induce secondary pollution and compete with the target pollutants to consume reactive oxygen species. For the additionally added heterogeneous co-catalysts, poor interactions between the co-catalysts and Fe components at the interface result in a vast transmission loss of electrons. In this scenario, to pursue an economical and high-efficiency PS-AOPs, the development of a novel strategy to construct heterogeneous Fe-based systems with rapid Fe^{3+}/Fe^{2+} cycle is very appealing.

Introducing Fe moieties into a suitable host via a lattice confinement strategy has been reported to be a facile method to generate efficient Fe-based catalytic systems for PS-AOPs [10,11]. This is because a host with specific components and morphology can not only tightly accommodate Fe moieties but also modulate the chemical environment and electronic structure of the Fe components, ultimately benefiting the Fe^{3+}/Fe^{2+} cycling [12,13]. Besides, an appropriate amount of Fe moieties dispersed in the host can also facilitate spatial separation and adequate exposure of the metal active centers [14,15]. Therefore, such configuration of Fe moieties constructed in a specific vehicle is highly promising for catalysis of persulfate activation. In this context, several Fe-doped

---

catalysts, such as Fe-POMs/TiO_2 [16], FeMgAl-MoS_4 [12], and Fe-g-C_3N_4 [17], have been developed to boost PS-AOPs for environmental remediation. However, these developed systems are still associated with inferior Fe^{2+} recovery owing to the weak chemical interaction between the Fe moieties and supports and the requirement of extra reducing agents. Moreover, the rigid chemical structures of the supports lead to limited accommodation of the Fe moieties and encumber further improvement in catalytic performance. As coordination structures have major advantages over traditionally rigid structures in terms of tunability [18,19], the development of an efficient Fe-based system for PS-AOPs by incorporating Fe moieties into coordination frameworks is highly attractive.

Metal-organic frameworks (MOFs), a type of coordination polymer, have many fascinating properties, such as large surface areas, uniform and tunable cavities, and tailorable chemistry [20,21]. As the constituents of MOFs can be readily tuned by varying the metal ions or bridging organic linkers, MOFs can serve as an interesting host for incorporation of Fe components to engineer efficient catalysts with heteroatomic metal nodes [22]. The strong coordination bonds formed between the embedded Fe moieties and ligands enable precise electron transmission and high chemical stability. Besides, previous studies have revealed that MOFs can be described as arrays of self-assembled and photoactive molecular catalysts [23]. This makes MOFs can be employed as solid ligands to excite Fe components via ligand-to-metal charge transfer under light irradiation, which substantially prevents the additional inclusion of reductants. These superiorities, combined with the open pore channels and rich nanoscale cavities of MOFs, might offer a rapid Fe^{3+}/Fe^{2+} cycling opportunity to Fe-incorporated MOFs to realize efficient PS-AOPs.

To verify this assumption, Fe-incorporated Ni-based MOFs (FeNi-MOFs) were prepared and used as stable catalyst for peroxodisulfate (PDS) activation and organic pollutant degradation under visible-light irradiation. In such a novel FeNi-MOFs system, Ni-based MOFs (Ni-MOFs) was chosen as host owing to its fully open pores, abundant accessible active sites, and redox potential matched well with that of Fe^{3+}/Fe^{2+} [24,25]. Spectral analyses demonstrated that Fe moieties were homogeneously incorporated and substituted a portion of Ni in the Ni-MOFs, forming FeNi-MOFs with heteroatomic metal nodes. Owing to the chemical coordination bonds and polarizations of the adjacent Ni centers, two pathways of precise electron transmission were revealed in FeNi-MOFs under visible-light irradiation, which promoted Fe^{2+} recovery with an Fe^{3+}/Fe^{2+} cycling efficiency greater than 58%. As a proof-of-concept, the resultant FeNi-MOFs delivered admirable catalytic performance in PDS conversion for organic pollutant degradation. Further, FeNi-MOFs showed specific activity as high as 92.6×10^{-4} $Lmin^{-1}m^{-2}$, which is 11.6-fold higher than that of the control Ni-MOFs/Fe^{3+} (7.95×10^{-4} $Lmin^{-1}m^{-2}$) system and superior to the existing catalysts reported to date. This work can deepen understanding of the Fe^{3+}/Fe^{2+} cycle process in Fe-incorporated systems and inspire the design of highly efficient Fe-based catalysts for PS-AOPs.

2. Experimental section

2.1. Preparations

All the reagents were commercially available and used without further purification. The FeNi-MOFs were synthesized from the solvothermal reactions of nickel acetate tetrahydrate (Ni(OAc)$_2$0.4 H_2O), ferric sulfate (Fe$_2$(SO$_4$)$_3$) and terephthalic acid (H$_2$BDC). Typically, Ni (OAc)$_2$0.4 H_2O (0.25 mmol, 62.2 mg) was dissolved in an aqueous solution (15 mL) containing a certain amount of Fe$_2$(SO$_4$)$_3$ under stirring conditions. Then, H$_2$BDC (0.125 mmol, 20.8 mg) dissolved in N,N-dimethylacetamide (15 mL) was then added dropwise to the above solution. After continuous stirring for 10 min, the resulting mixture was transferred to a Teflon-lined stainless steel vessel and heated at 150 °C for 3 h. Once the autoclaved solution had cooled, the product was isolated from the supernatant by decanting, washed with water and methanol and dried overnight at 60 °C in an oven. FeNi-MOFs with different Fe/Ni mole ratios were prepared by tuning the dosage of Fe$_2$(SO$_4$)$_3$. For comparison, bare Ni-MOFs were also synthesized according to the synthetic procedures for FeNi-MOFs except that no Fe$_2$(SO$_4$)$_3$ was added. The MIL-101(Fe), an Fe-based MOFs with a similar composition and topology to the FeNi-MOFs, was prepared according to a previously reported procedure [26].

2.2. Characterizations

The samples were characterized by X-ray diffraction (XRD) using Bruker D8 Advance X-ray diffractometer with Cu K$_a$ radiation (λ = 1.5406 Å) at a scanning rate of 2°/min in the 2θ range between 5° and 35°. UV–visible diffuse reflectance spectra (UV–vis DRS) of the samples were obtained using BaSO$_4$ as a reflectance standard. Fourier transform infrared spectroscopy (FTIR) spectra were obtained using a Bruker spectrometer in a KBr pellet. BET surface areas were determined on an ASAP 2020 M apparatus (Micromeritics Instrument Corp., USA). The scanning electron microscopy (SEM) images were collected with a Nova Nano SEM 230 microscope. Transmission electron microscopy (TEM) images were obtained on a JEOL model JEM 2010 EX instrument. Atomic Force Microscope (AFM) was performed to measure height profile of sample. X-ray photoelectron spectroscopy (XPS) measurements were performed on a PHI Quantum 2000 XPS system (PHI, USA). The ^{57}Fe Mössbauer spectra were recorded on an SEE Co W304 Mössbauer spectrometer, using a ^{57}Co/Rh source in transmission geometry. Inductively coupled optical emission spectrometry (ICP-OES) was performed on Optima 8000 (PerkinElmer).

2.3. Degradation experiments

Degradation experiments were carried out in a 100 mL glass reactor containing 50 mL of the solution at room temperature with magnetic stirring. To avoid any misleading results, buffer reagents were not used and the pH of the solution was not further adjusted unless otherwise stated. In typical procedures, a 0.2 g/L catalyst was suspended in tetracycline (TC) solution (30 mg/L, 50 mL). The degradation was initiated by the addition of 1.5 mmol/L PDS and exposed to a 300 W xenon lamp with a 420 nm light filter at the same time. The light intensity is 98 mW/cm^2. At a predetermined time interval, 1.0 mL of the reaction solution was withdrawn and immediately quenched using 0.5 mL anhydrous methanol. The reaction mixture was centrifuged and the supernatant was analyzed by HPLC to determine the residual TC. The experimental operations of carbamazepine (CBZ), bisphenol A (BPA), rhodamine B (RhB), and methyl orange (MO) degradations were similar to that of TC. The PDS concentration was monitored spectrophotometrically as reported in our previous work. Specific activity was determined via the rate constant normalized to the specific surface area and concentration of the catalyst [27]. All experiments were tested three times, and the averaged values were reported with standard deviations.

A steady-state kinetic model was established in a mixed system containing TC, nitrobenzene (NB) and benzoic acid (BA). The competitive reactions of TC, NB and BA degradations were performed under typical reaction conditions over FeNi-MOFs/PDS. The kinetic equations of NB, BA and TC removal were expressed as Eqs. (1)–(3), and the contributions (R) of·SO$_4$ and·OH to TC degradation were calculated according to the formulas (Eqs. (4)–(5)) [28].

$$\ln \frac{[NB]}{[NB]_0} = -k_{\cdot OH,NB} \quad [\cdot OH]_{ss} t = -k_{obs,NB} t \tag{1}$$

$$\ln \frac{[BA]}{[BA]_0} = -(k_{\cdot OH,BA} \quad [\cdot OH]_{ss} + k_{SO_4^-,BA} \quad [SO_4^-]_{ss})t = -k_{obs,BA} t \tag{2}$$

$$\ln\frac{[\text{TC}]}{[\text{TC}]_0} = -k_{\text{obs,TC}}t \tag{3}$$

$$R_{\cdot\text{OH}} = \frac{k_{\cdot\text{OH,TC}} \quad [\cdot\text{OH}]_{\text{ss}}}{k_{\text{obs,TC}}} \tag{4}$$

$$R_{\text{SO}_4^{\cdot-}} = \frac{k_{\text{SO}_4^{\cdot-}} \quad [\text{SO}_4^{\cdot-}]_{\text{ss}}}{k_{\text{obs,TC}}} \tag{5}$$

Where $[\text{NB}]_0$, $[\text{BA}]_0$, $[\text{TC}]_0$, $[\text{NB}]$, $[\text{BA}]$ and $[\text{TC}]$ represented the initial and transient concentrations of NB, BA and TC, respectively. $[\cdot\text{OH}]_{\text{ss}}$ and $[\text{SO}_4^{\cdot-}]_{\text{ss}}$ were the steady-state concentrations of $\cdot\text{OH}$ and $\text{SO}_4^{\cdot-}$, respectively. The $k_{\cdot\text{OH}}$ and $k_{\text{SO}_4^{\cdot-}}$ were the standard kinetic constants of $\cdot\text{OH}$ and $\text{SO}_4^{\cdot-}$, which were presented in Table S1.

### 2.4. Density functional theory (DFT) calculations

Density functional theory (DFT) calculations were carried out to study the dynamic cycle process of Fe^{3+}/Fe^{2+} cycling in FeNi-MOFs. All the calculations were performed using the Vienna ab initio simulation package (VASP) and the generalized gradient approximation (GGA) within Perdew-Burke-Ernzerhof (PBE) formulation was utilized for exchange-correlation energy [29]. The projected augmented wave (PAW) potentials were chosen to describe the ionic cores and take valence electrons into account using a plane wave basis set with a kinetic energy cutoff of 450 eV. Partial occupancies of the Kohn−Sham orbitals were allowed using the Gaussian smearing method with a width of 0.05 eV. The electronic energy was considered self-consistent when the energy change was smaller than 10^{-5} eV. A geometry optimization was considered convergent when the force change was smaller than 0.05 eV/Å. Grimme's DFT-D3 methodology was used to describe the dispersion interactions. The Brillouin zone was sampled with $3 \times 3 \times 1$ Monkhorst-Pack k-points grids. The Hubbard U parameters of Ni, Fe were chosen to be 3.85 and 4.95 eV, respectively.

3. Results and discussion

3.1. Characterization of samples

Ni-MOFs, a two-dimensional MOF material, is chosen as platform for accommodating Fe components due to its high water-resistance and redox potential matched well with that of Fe^{3+}/Fe^{2+} [30,31]. Its topological structure is shown in Fig. S1. The Fe-modified Ni-MOFs (FeNi-MOFs) are prepared via the solvothermal reaction of $Ni(OAc)_2$, $Fe_2(SO_4)_3$ and H_2BDC. The obtained sample shows XRD patterns and FTIR spectra similar to the pristine Ni-MOFs and the calculated one (CCDC No. 638866) (Fig. 1a and S2), confirming that the introduction of Fe components does not destroy the Ni-MOF framework structure [24]. Only a small amount of the heterogeneous MOF crystalline phase (CCDC No. 985792) is observed as evidenced by the shoulder peak at $2\theta = 8.9°$, indicating the high quality of the as-obtained Ni-MOFs and FeNi-MOFs. No peaks assigned for iron oxides are detected in the XRD patterns. However, the diffraction peak of Ni-MOFs at $2\theta= 9.3°$ shows a left-shift after the bringing of the Fe species, demonstrating the successful incorporation of Fe into the FeNi-MOF materials (Fig. 1a inset) [32]. To confirm this incorporation, XPS analysis is conducted on the FeNi-MOFs. The XPS survey spectrum discloses the presence of C, O, Ni, and Fe elements in the FeNi-MOFs (Fig. S3a). No obvious difference is observed in the C 1 s and O 1 s XPS spectra of both FeNi-MOFs and Ni-MOFs (Fig. S3b,c). The high-resolution XPS spectrum of Ni can be deconvoluted into two peaks at 855.9 and 873.5 eV, which are assigned to Ni^{2+} (Fig. S3d). While a upshift by 0.5 eV is observed after the addition of Fe components, which may be induced by the polarization effect between Fe and Ni components [33]. In the case of Fe, the characteristic peaks at 713.9 and 727.3 eV in the spectra of FeNi-MOFs can be attributed to
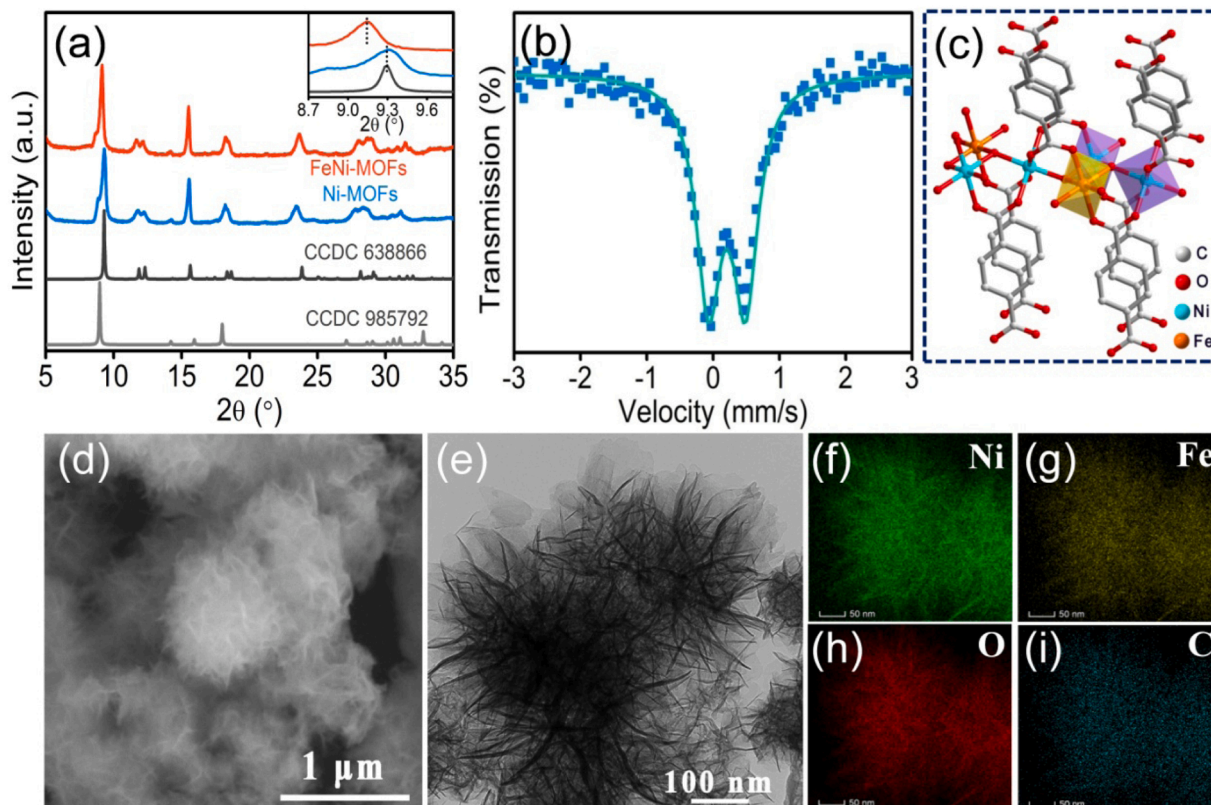
Fig. 1. (a) XRD patterns of synthesized FeNi-MOFs, Ni-MOFs and calculated Ni-MOFs. (b) Mössbauer spectrum of FeNi-MOFs. (c) Proposed crystal structure of FeNi-MOFs. (d) SEM, (e) TEM and (f-i) EDS elemental mapping of FeNi-MOFs.

Fe^{3+} $2p_{3/2}$ and $2p_{1/2}$, respectively (Fig. S3e) [34]. Interestingly, the peak of Fe shifts to a lower binding energy after immobilization in the Ni-MOF frameworks as compared to that of the Fe salt. Such reversed shifts in the binding energies of Ni 2p and Fe 2p infer a strong interplay between the Ni and Fe components in FeNi-MOFs with an internal electron transfer from Ni^{2+} to Fe^{3+}, benefiting the Fe^{3+}/Fe^{2+} redox cycle.

To accurately investigate the electronic structure of the Fe components in the FeNi-MOFs, Mössbauer spectroscopy is also performed. As displayed in Fig. 1b, one quadrupole doublet can be adequately simulated by a single Lorentzian line, manifesting a highly uniform chemical environment of Fe^{3+} [35]. The absorption peaks of the simulated doublet exhibit an isomer shift (IS) of 0.21 mm/s relative to that of metallic α-Fe, which can be assigned to a typical high-spin Fe^{3+} octahedrally coordinated by oxygen atoms (FeO_6). Further, a high quadrupole splitting (QS) value of 0.56 mm/s is obtained, further verifying the chemical statement of Fe^{3+} in a FeO_6-type octahedral site [36]. This result, together with the abovementioned characterizations, demonstrates that Fe components have incorporated into Ni-MOF frameworks and substituted a portion of Ni to form FeNi-MOFs with heteroatomic

metal-oxo nodes. And the crystal structure of the FeNi-MOFs can be deduced and displayed in Fig. 1c. The Fe content of the FeNi-MOFs is 2.3 wt% based on ICP-OES analysis.

The morphology of the resultant FeNi-MOFs is characterized using SEM and TEM measurements. A marigold-shaped morphology composed of many laminas is observed over the FeNi-MOFs, in contrast to the pure Ni-MOFs with scattered nanosheet-like structure (Fig. 1d and S4). The edges of the laminas in the FeNi-MOFs display some wrinkles, verifying the lamelliform structure. Obvious corrugation and faint contrast of the laminas are also observed in the TEM images, indicating the ultrathin nature of the FeNi-MOFs (Fig. 1e). The thickness of the laminas in FeNi-MOFs is measured in the range from 1.73 nm to 3.63 nm according to the AFM measurements (Fig. S5). EDX elemental mapping shows a uniform dispersion of C, O, Ni and Fe (Fig. 1f-i). Notably, the distribution of Fe in FeNi-MOFs align with that of Ni, showing homogeneous incorporation of the Fe components in the FeNi-MOF framework and in line with the results of XPS and Mössbauer spectroscopy analyses. The surface area of the FeNi-MOFs is 41.2 m^2/g, which is ca. 1.6 times higher than that of the Ni-MOFs (25.8 m^2/g) (Fig. S6). The
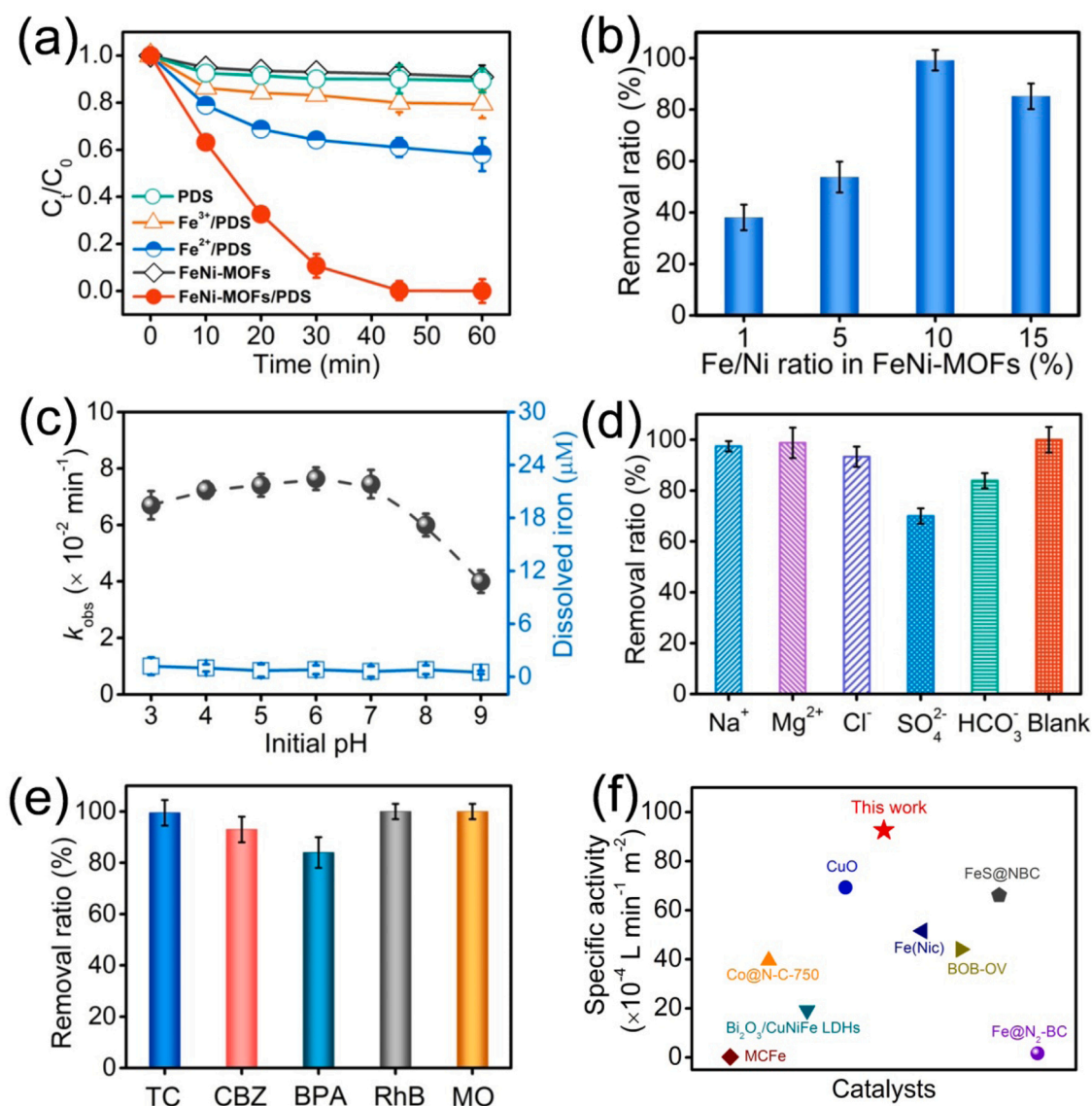
Fig. 2. (a) Degradation rate of TC over different systems. (b) Effect of Fe/Ni ratio on TC degradation rate. (c) Effect of pH on TC degradation rate and total dissolved iron concentration. (d) Effect of inorganic ions on TC degradation in FeNi-MOFs/PDS system. (e) Capability of the FeNi-MOFs/PDS system for degrading various pollutants. (f) Specific activity comparisons of FeNi-MOFs and existing catalysts. Experimental conditions: [pollutant]$_0$ = 30 mg/L; [Catalyst]$_0$ = 0.2 g/L; [PDS]$_0$ = 1.5 mM; [inorganic ions]$_0$ = 5 mM.

UV–vis DRS spectrum of FeNi-MOFs shows higher light absorption capacity in the range of 200–600 nm relative to that of Ni-MOFs, owing to the existence of extra charge transfer after Fe incorporation (Fig. S7). These results demonstrate that FeNi-MOFs supposes to be an efficient catalyst for photoinduced persulfate activation. For comparison, MIL-101(Fe) is prepared and well characterized by XRD pattern, N_2 adsorption/desorption isotherms and TEM measurements as shown in the Supporting Information (Fig. S8) [26].

3.2. Catalytic performance of FeNi-MOFs

The catalytic performance of the resultant FeNi-MOFs is assessed for the activation of the PDS oxidant for TC degradation under visible light. As shown in Fig. 2a, a rather limited TC removal rate is obtained in the presence of individual PDS and FeNi-MOFs after irradiation for 60 min. Notably, complete TC degradation, with a TOC removal rate of 58.5%, is fulfilled when PDS is added in the presence of FeNi-MOFs. The TON and TOF based on Fe active sites are calculated to be 0.83 and 0.014 min^{-1}, respectively. However, only 15% of TC is eliminated by the Ni-MOFs in the presence of PDS after illumination, demonstrating that Fe species play a key role in the PDS activation for TC degradation over FeNi-MOFs (Fig. S9). The pure Fe-based MOFs (MIL-101(Fe)) shows inferior TC removal rate (31%) to the FeNi-MOFs under similar conditions, suggesting the existence of synergy between the Fe components and the Ni-MOFs matrix (Fig. S10). Light irradiation also plays an important role in PDS activation as less than 40% of TC is removed in the FeNi-MOFs/PDS system in the absence of light (Fig. S9), aligning with the deduction of the photoactive performance (Fig. S11). Impressively, FeNi-MOFs/PDS delivers even higher TC degradation than the homogeneous Fe^{2+}/PDS and Fe^{3+}/PDS systems, highlighting the admirable catalytic activity of irradiated FeNi-MOFs in PDS activation for organic pollutant degradation (Fig. 2a).

To optimize the reaction conditions, the key reaction parameters for TC degradation, including the concentrations of FeNi-MOFs, PDS oxidant, and pH on the TC degradation, are investigated. The TC removal rates are linear with respect to both PDS and FeNi-MOFs at relatively low concentrations, but plateaued or declined at their higher values (Fig. S12). The sluggish degradation kinetics at higher concentrations of FeNi-MOFs and PDS oxidant could be due to reactive oxygen species scavenging by excess substrates or catalyst. The highest TC degradation rate is gained when the FeNi-MOFs and PDS concentrations are fixed at 0.2 g/L and 1.5 mmol/L, respectively. In addition, the catalytic performance is found to be significantly influenced by FeNi-MOFs with different Fe/Ni mole ratio. A volcano-shaped curve with the maximum TC removal rate at an Fe/Ni mole ratio of 1:10 is observed (Fig. 2b). The FeNi-MOFs exhibits an unexpectly high catalytic activity over a wide pH range of 3.0–9.0. An optimal TC removal rate with a maximum apparent kinetic constant ($k_{obs} = 7.63 \times 10^{-2}$ min^{-1}) is found at pH = 6.0, coinciding closely with the real pK_a of TC (7.7) (Fig. 2c) [37]. The curve is found to tail on the high-pH side due in part to the self-hydrolyzation of PDS [38]. Furthermore, the constructed FeNi-MOFs/PDS system exhibits an excellent anti-interference ability. Although excess SO_4^{2-} and HCO_3^- induce slight inhabitation, the introduction of inorganic ions ubiquitous in environmental waters, including Na^+, Mg^{2+}, and Cl^-, exerts negligible effect on TC degradation (Fig. 2d). These results indicate potential matrix effects in environmental water samples and serve as additional proof of the essential role played by FeNi-MOFs in the efficient activation of persulfate. The degradation intermediates and final products are identified by high performance liquid chromatography-mass spectrometry. As shown in Fig. S13, the small fragments are observed, and the proposed structures are summarized in Table S1. In addition, experiments on the environmental exposure of Daphnia magna indicate that the intermediate products of TC degradation are markedly less toxic than TC (Fig. S14). These results indicate that FeNi-MOFs/PDS is promising for wastewater treatment.

FeNi-MOFs/PDS exhibits remarkable activity for the removal of other refractory contaminants. Almost complete degradations of CBZ, RhB, and MO are achieved with considerable k_{obs} (0.11–0.046 min^{-1}) within 60 min (Fig. 2e and S15). Despite the inferior degradation rate of BPA, more than 85% of the BPA is still removed when the reaction time is prolonged to 90 min. These results suggest a wide capability of FeNi-MOFs for PDS activation in wastewater management. To better understand the reactive characteristics of the system, the specific activity is adopted to reflect the intrinsic catalytic activity. According to the apparent kinetics and surface areas of the FeNi-MOFs, the specific activity of the FeNi-MOFs/PDS is calculated to be 92.6×10^{-4} Lmin^{-1}m^{-2}. This is 11.6 times higher than that of the Ni-MOFs/PDS (7.95×10^{-4} Lmin^{-1}m^{-2}), indirectly highlighting the superiority of the Fe dopants in FeNi-MOFs for PDS activation. Following this principle, the catalytic activity of PDS activation and organic pollutant degradation is compared between FeNi-MOFs and state-of-the-art catalysts. As illustrated in Fig. 2f, the intrinsic specific activity of the FeNi-MOFs is observably greater than that of the existing catalysts reported to date, proving that the FeNi-MOFs is among the ranks of excellent PDS activators [39–46]. This finding aligns with the result of modified kinetic constant k_m (the k_{obs} divided by catalyst dosage) versus the mole ration of the PDS/TC profile (Fig. S16). Moreover, the FeNi-MOFs also shows high stability for PDS activation. Only a slight decrease in activity is observed for the FeNi-MOFs/PDS system after six consecutive cycles (Fig. S17). ICP analysis of the filtrate reveals no detectable Fe and Ni. The FeNi-MOFs after six runs shows nearly the same XRD patterns, FTIR and TEM images, suggesting that the crystal phase and the morphology of FeNi-MOFs are still maintained (Fig. S18-S20). These results indicate that the FeNi-MOFs are highly efficient and stable catalyst for PDS activation and decontamination.

3.3. Identification of active species and quantitative contributions

The major reactive oxygen species in the TC degradation process are explored first through quenching experiments. A negligible influence on the TC removal rate is observed when superoxide dismutase (SOD) and furfuryl alcohol (FFA) are added into the FeNi-MOFs/PDS system. In contrast, MeOH and TBA severally decrease the TC degradation rate from ~100–37.2% and 49.8%, respectively (Fig. 3a and S21). Further, the corresponding k_{obs} are reduced from 7.63×10^{-2} min^{-1} to 1.21×10^{-2} min^{-1} for MeOH and 1.72×10^{-2} min^{-1} for TBA, respectively [47]. Therefore, hydroxyl (·OH) and sulfate (·SO$_4^-$) radicals, rather than·O$_2^-$ and ^{1}O$_2$, are the main active species for TC degradation. The generation of·OH and·SO$_4^-$ in the FeNi-MOFs/PDS system is further identified by 5,5-dimethyl-1-pyrroline N-oxide (DMPO)-trapped EPR experiments. No peaks are detected in the presence of PDS and FeNi-MOFs alone under light irradiation, indicating that almost no radicals are produced. However, strong quadruple peak signals of the DMPO-·OH adducts are observed when FeNi-MOFs is suspended in the PDS solution under light irradiation, indicating the production of·OH radicals in the irradiated FeNi-MOFs/PDS system (Fig. 3b) [48,49]. In addition, extremely weak sextet peaks assigned to DMPO-·SO$_4^-$ adducts are also observed, suggesting that a small amount of·SO$_4^-$ is also involved in the oxidative system [50,51]. Of note, the peak intensities of the DMPO-·OH and DMPO-·SO$_4^-$ adducts increase along the irradiation time, obviously evidencing the existence of·OH and·SO$_4^-$ in the illuminated FeNi-MOFs/PDS system. The cumulative generation of·OH in FeNi-MOFs/PDS is measured according to the classical chemical probe method using terephthalic acid (TPA) as the probe molecule. As shown in Fig. 3c, TPA is readily converted to hydroxyterephthalic acid (hTPA) in the irradiated FeNi-MOFs/PDS system. And the concentration of hTPA is increased with the decrease of PDS concentration. This result experimentally illustrates that the generation of·OH is derived from the PDS depletion and its concentration reaches up to ca. 21.5 μmol/L after 60 min. Previously, the formation of ferryl species is reported in several Fe-containing PDS activation systems, which are able to oxidize sulfoxides to sulfones [52]. However, dimethyl sulfoxide (DMSO) and
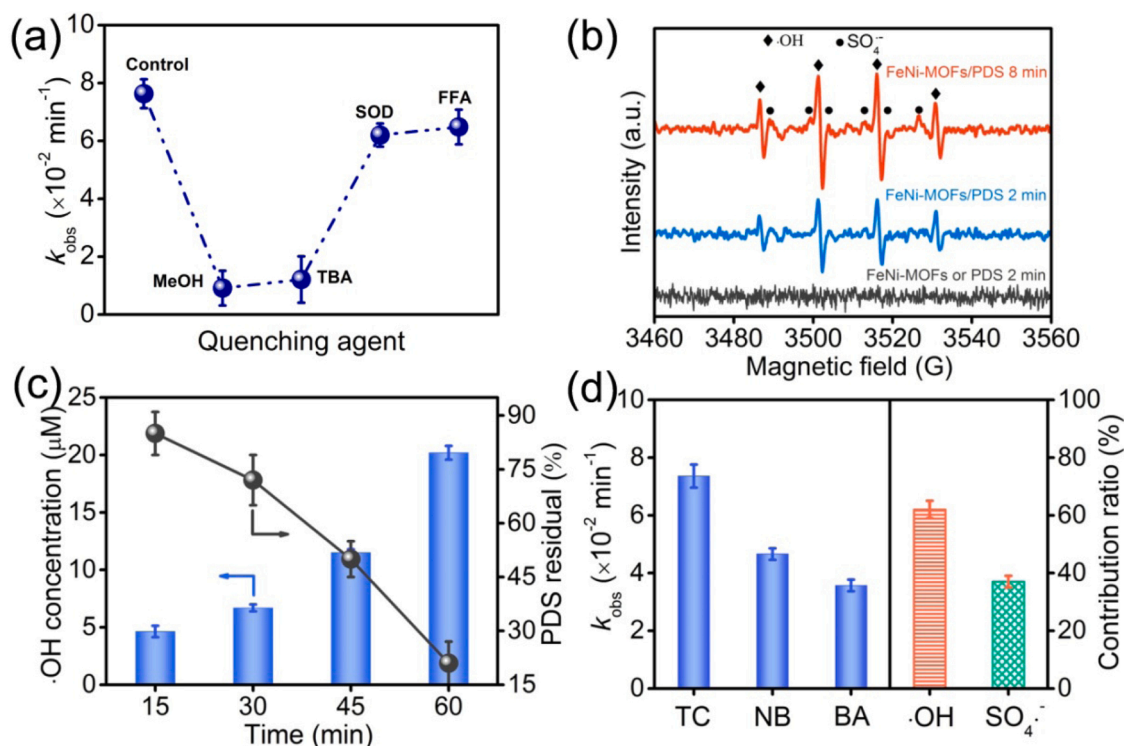
Fig. 3. (a) Quenching experiments on TC degradation. (b) DMPO-trapped EPR spectra of PDS activation over FeNi-MOFs, PDS and FeNi-MOFs/PDS under light irradiation. (c) Formation kinetics f ·OH and PDS consumption. (d) Reaction kinetics of TC, NB and BA over FeNi-MOFs/PDS system and the contribution of·OH and SO_4^- toward TC degradation. Experimental conditions: $[TC]_0 = [NB]_0 = [BA]_0 = 30$ mg/L; $[Catalyst]_0 = 0.2$ g/L; $[PDS]_0 = 1.5$ mM; $[quencher]_0 = 750$ mM; $[TPA]_0 = 2$ mM.

phenyl methyl sulfoxide (PMSO) do not interfere with TC degradation and the characteristic phenyl methyl sulfone ($PMSO_2$) byproduct is not detected. These results strongly against the involvement of ferryl species in the TC degradation.

To distinguish and quantify the contributions of·OH, ·SO_4^- and other undetectable species to TC degradation, competition kinetics experiments are carried out based on steady-state kinetic model (Fig. 3d). NB and BA chemical probes are chosen owing to their different thermodynamics oward ·OH and·SO_4^- as compared with TC (Table S2). According to the Eqs. (1)–(2), the steady-state concentrations of·OH and·SO_4^- are calculated to be 1.77×10^{-7} and 2.01×10^{-6} μmol/L, respectively. Thus, the estimated relative contribution of·OH to TC oxidation in the FeNi-MOFs/PDS system is 61.8%, which is higher than that of·SO_4^- (37.4%). These results highlights the main functions of·OH and·SO_4^- in TC degradation, in consistent with the results of quenching experiments.

The interactions between·OH,·SO_4^- and FeNi-MOFs are further investigated. Previous studies revealed that·SO_4^- with high oxidation potential can react with H_2O molecules to produce·OH. However, the reaction rate constant is very low ($k < 2 \times 10^{-3}$ s^{-1}) [53]. Interestingly, coordinated H_2O in MOFs has recently reported to show the potential ability to tune the transformation of·SO_4^- to·OH production [47]. As coordinated H_2O exists in the FeNi-MOFs, the catalytic tuning effect of coordinated H_2O is assumed to play a role in transferring·SO_4^- to·OH in the FeNi-MOFs/PDS system. To confirm it, experiments on the substitution of coordinated H_2O with phosphate anions and the classical chemical probe method using TPA as a probe molecule are conducted [54]. As shown in Fig. S22, the transformation efficiency of TPA to hTPA is significantly inhibited as the phosphate concentration increased from 0 to 10 mg/L. Less than 18% of hTPA is obtained in the presence of 10 mg/L phosphate in FeNi-MOFs/PDS relative to that of the control one. This result clearly indicates the regulation effect of coordinated H_2O in the FeNi-MOFs on transferring·SO_4^- to·OH production.

3.4. Iron cycle and reaction mechanism

To unravel the high-activity origin of the FeNi-MOFs in PDS activation and organic pollutant degradation, controlled experiments on Ni-MOFs and the Fe components for PDS activation are carried out. The Fe^{3+}/PDS and Ni-MOFs/PDS systems show inferior activities toward TC degradation, while moderate removal rate of TC is observed in Fe^{2+}/PDS system (Fig. 2a and S9). These results indicate that either the heterogeneous Ni-MOFs or homogeneous Fe^{3+} is inappropriate for PDS activation under the current conditions. However, the degradation efficiency of TC is significantly improved and even higher than that of Fe^{2+}/PDS system when Ni-MOFs is added in the Fe^{3+}/PDS (Fig. S23). This result might be due to the acceleration of iron cycling by Ni-MOFs. Therefore, instantaneous Fe^{2+} concentrations in the reactive systems are determined using the modified phenanthroline method (Fig. 4a). A shape decrease in Fe^{2+} concentration is found in the Fe^{2+}/PDS system after 10 min, whereas complete consumption is observed when the reaction is extended to 15 min. This finding indicates that Fe^{2+} can rapidly react with and activate PDS. Meanwhile, a negligible amount of Fe^{2+} was detected throughout the irradiated Fe^{3+}/PDS system, suggesting that Fe^{3+} can not be chemically reduced to Fe^{2+} in the presence of PDS and light irradiation. Notably, when Ni-MOFs cocatalysts are introduced, the regeneration of Fe^{2+} occurs and the concentration of Fe^{2+} slightly increases in 15 min. Thus, stabilization at approximately 0.058 mmol/L occurs in the next 60 min and the Fe^{2+} regeneration rate reaches 58% in the Ni-MOFs/Fe^{3+}/PDS system, indicating that Ni-MOFs can really reduce the Fe^{3+} under light irradiation. Moreover, the comparable TC removal performance of the Ni-MOFs/Fe^{3+}/PDS system in relative to the FeNi-MOFs/PDS system also confirms the efficient reduction of Fe^{3+} (Fig. S23). In addition, the continuous decomposition of PDS reaches 78% in Ni-MOFs/Fe^{3+}/PDS system within 60 min and slightly lower than that in FeNi-MOFs/PDS system (82%) but much higher than that in the Fe^{2+}/PDS system (42%). On the basis of these
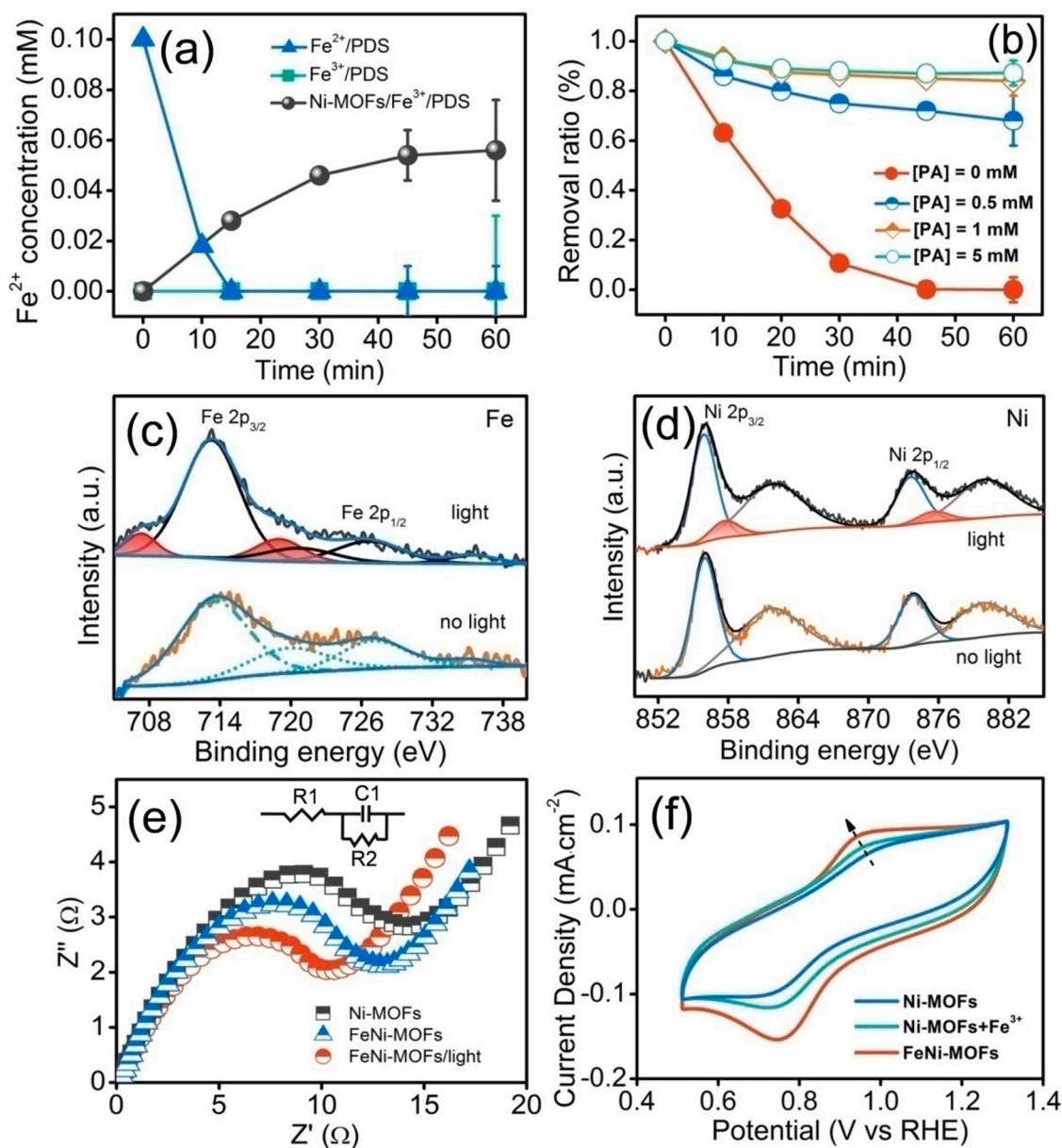
Fig. 4. (a) The concentration of Fe^{2+} over different systems. (b) The quenching effect of TC removal rate in FeNi-MOFs/PDS system. (c,d) The XPS spectra of Fe and Ni in FeNi-MOFs with or without light irradiation. (e) The electrochemical impedance spectra. (f) Cyclic voltammetry measurements over different systems. Experimental conditions: $[TC]_0$ = 30 mg/L; $[catalyst]_0$ = 0.2 g/L; $[PDS]_0$ = 1.5 mM; $[Fe^{2+}]_0$ = $[Fe^{3+}]_0$ = 4.6 mg/L.

experiments and discussions, the superior performance of FeNi-MOFs in PDS activation can also be attributed to accelerated Fe^{3+}/Fe^{2+} cycling.

To gain insight into the Fe^{3+}/Fe^{2+} cycling in FeNi-MOFs, phenanthroline quenching experiments are conducted. A significant inhibition of TC degradation and a pink-colored suspension are observed when phenanthroline is introduced into the FeNi-MOFs/PDS system (Fig. 4b). This phenomenon indicates that Fe^{2+} is substantially formed in the FeNi-MOFs during the reaction. The reduction potential of Fe^{3+} in FeNi-MOFs is further illustrated by the in situ XPS measurements under visible light irradiation. As shown in Fig. 4c, the high-resolution XPS spectra of Fe reveal two peaks at 713.6 and 727.1 eV over FeNi-MOFs with or without light irradiation, which are assigned to Fe^{3+}. Interestingly, two new peaks at 707.2 and 719.3 eV in the spectra of Fe 2p are deconvoluted after irradiation, which is attribute to reduced Fe^{2+} [55]. In the Ni 2p spectra, additional peaks assigned to Ni^{3+} in the after-irradiated FeNi-MOFs are observed as compared with those without light irradiation (Fig. 4d) [56]. Such reverse valence conversion of Ni and Fe in the

after-irradiated FeNi-MOFs indicates that Ni^{2+} can be oxidized and can donate electrons to Fe^{3+} to generate reduced Fe^{2+}. It is hypothesized that the reduction of Fe^{3+} via the electron transfer from Ni^{2+} requires additional energy, such as light energy, as no reduction reaction occurs in the FeNi-MOFs in the absence of light irradiation. Upon light irradiation, the electrons around the Ni^{2+} suppose to be excited and overcome the energy barrier to reach neighboring Fe^{3+}, which is also evidenced by the reduced electrochemical impedance, photoluminescence and photocurrent measurements (Fig. 4e and S24). Notably, the reductive reaction between Ni^{2+} and Fe^{3+} in FeNi-MOFs in the presence of extra energy seems more convenient than that in the Ni-MOFs/Fe^{3+} system. Cyclic voltammetry measurements demonstrate that the oxidation potential of Ni^{2+}/Ni^{3+} in FeNi-MOFs shifts to a lower value as compared with that in the Ni-MOFs/Fe^{3+} system, however they are both smaller than that of bare Ni-MOFs (Fig. 4f). These results manifest that Ni^{2+} is favor for electron-donating to reduce Fe^{3+}, which makes FeNi-MOFs efficient catalyst for PDS activation.

Density functional theory (DFT) calculations further reveal the dynamic cycle process of Fe^{3+}/Fe^{2+} cycling in FeNi-MOFs. The optimal structures of the Ni-MOFs, Ni-MOFs/Fe^{3+} and FeNi-MOFs are shown in Fig. S25. The charge density difference is firstly simulated in order to investigate the electronic structure of FeNi-MOFs. As shown in Fig. 5a and 5b, an overt charge accumulation around the Fe species and charge depletion around Ni components in the FeNi-MOFs system are clearly observed as compared with those in the Ni-MOFs/Fe^{3+} system. This result indicates that the electronic structures of both Fe and Ni in the FeNi-MOFs are modulated and exhibit vigorous interactions with each other, which is corroborated by the XPS results. More precisely, the Bader charge analyses exhibit a charge transfer of $0.27e^-$ from the surrounding Ni atoms to Fe species in FeNi-MOFs, while for Ni-MOFs/Fe^{3+}, it is only $0.11e^-$. The results vividly suggest that Fe species in the FeNi-MOFs are more conducive to obtain electrons and facilitate to trigger the subsequent reduction reactions. To further elucidate the origin of the improved Fe^{3+}/Fe^{2+} cycling efficiency in the FeNi-MOFs, the density of states (DOS) was also calculated to deeply investigate the changes in the electronic structure of the catalyst. The projected DOS (PDOS) calculations demonstrate that the degree of electron overlap of the Fe 3d orbital, O 2p orbital and Ni 3d orbital in the used FeNi-MOFs is larger than that in the used Ni-MOFs/Fe^{3+} (Fig. 5c and S26), which represents a stronger interaction and easier electron transfer in FeNi-MOFs. Besides, the D-band center of Fe in the FeNi-MOFs is more closer to the Fermi level than the D-band center of Ni in the FeNi-MOFs, corresponding to a stronger PDS adsorption on Fe sites in the FeNi-MOFs (Fig. 5d). This result is consistent with the calculated comparison of

the adsorption energies of the Fe and Ni sites for PDS (Fig. S27 and Table S3). The above results prove that the electronic configuration of the Ni components of Ni-MOFs can be modulated by Fe incorporation, which is beneficial for Fe^{3+}/Fe^{2+} redox recycling.

Based on the above analyses, the mechanism of enhanced photoinduced PDS activation for organic pollutant degradation over FeNi-MOFs is schematically illustrated in Fig. 6. Previous reports on Fe-containing MOFs revealed that an excited charge separation state occurs by transferring an electron from O^{2-} to Fe^{3+} in the Fe-O clusters upon visible light excitation. Accordingly, Fe^{3+} is reduced to Fe^{2+} (path I), which can activate the PDS. For the FeNi-MOFs, in addition to the direct excitation of Fe−O clusters, a second pathway exists via the excitation of the Ni-MOFs, followed by an electron transfer from excited Ni^{2+} species to the Fe^{3+} and then generate Fe^{2+} (path II). Ni^{2+} is oxidized to Ni^{3+}, which can extract electrons from organic pollutants to fulfill the cycle. Such an excitation pathway is similar to that observed for the previously reported MIL-100(Fe). The Ni-MOF components in FeNi-MOFs not only perform pivotal functions as a support for Fe component accommodation, but also as a heterogeneous ligand to activate Fe species under light irradiation. These two pathways can play synergistic roles in the excitation of FeNi-MOFs for highly efficient PDS activation and organic pollutant decontamination.
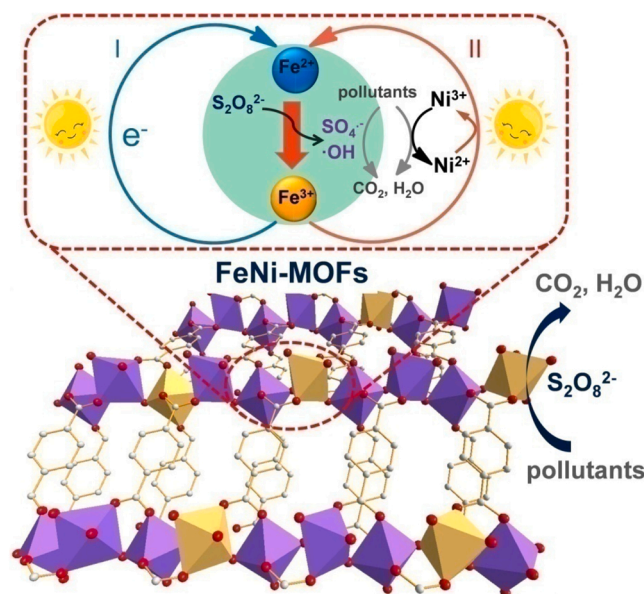
4. Conclusion

In summary, Fe-incorporated Ni-based MOFs (FeNi-MOFs) were prepared in this work and introduced into persulfate activation to
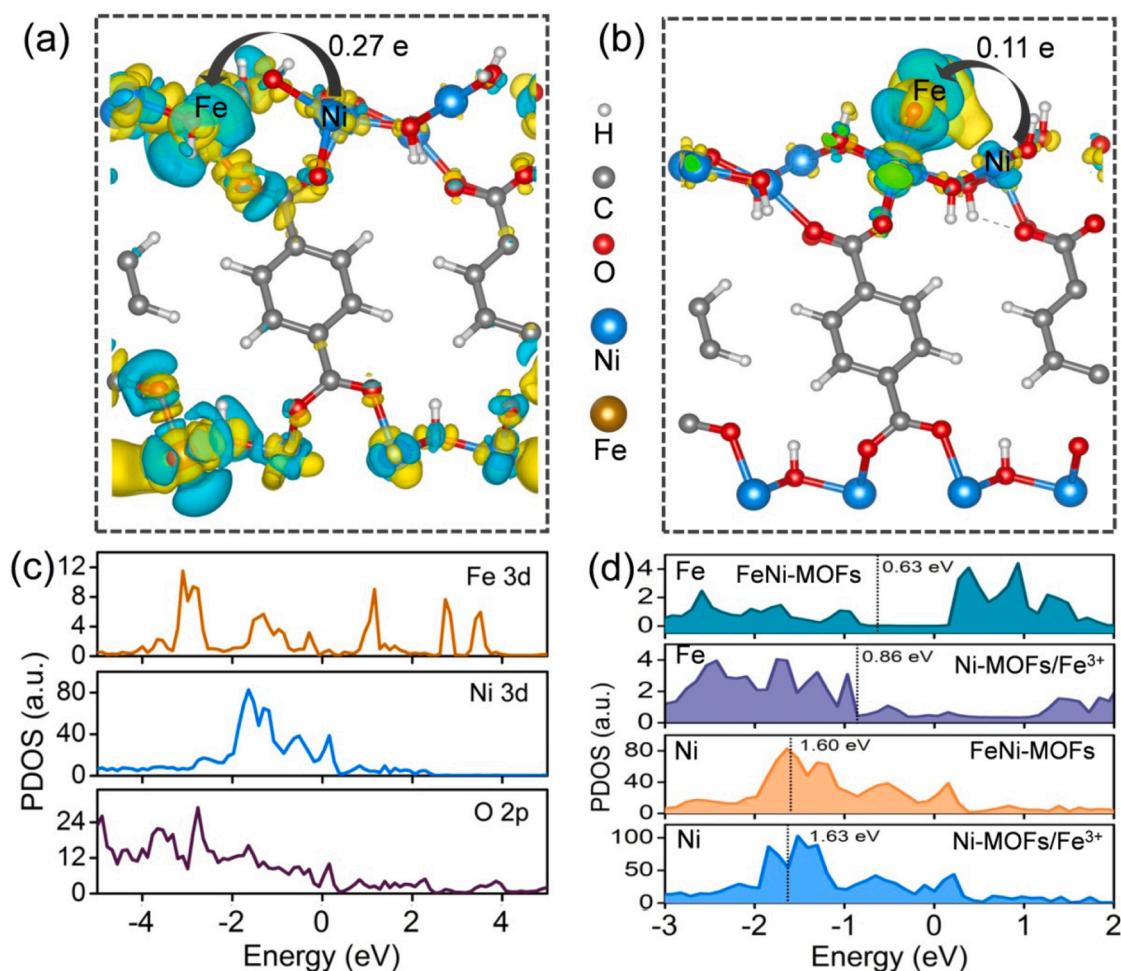
Fig. 5. (a and b) Difference charge densities of FeNi-MOFs and Ni-MOFs/Fe^{3+}. (c) The PDOS of FeNi-MOFs. (d) The PDOS of Fe and Ni moieties in different materials. The D-band centers are marked in the PDOS curves.

Fig. 6. The schematical illustration of Fe^{3+}/Fe^{2+} cycle and persulfate activation for pollutant degradation over FeNi-MOFs under light irradiation.

establish highly efficient PS-AOPs. Spectral analyses clarified the uniform incorporation of Fe moieties in Ni-MOFs, generating FeNi-MOFs with heteroatomic metal nodes. Under the help of ligand-to-metal charge transfer and polarizations of adjacent Ni centers, the as-formed FeNi-MOFs were subjected to precise electron transmission, benefiting Fe^{2+} recovery with an Fe^{3+}/Fe^{2+} cycling efficiency larger than 58%. As a result, the FeNi-MOFs showed excellent catalytic performance in PDS activation and organic pollutant degradation. In addition, the FeNi-MOFs exhibited a significantly higher specific activity than that of the control Ni-MOFs/Fe^{3+} and the state-of-the-art catalysts reported to date. This study reveals the intrinsic mechanism of the accelerated Fe^{3+}/Fe^{2+} redox cycle in a heterogeneous catalyst for persulfate activation and provides new insights into the design and synthesis of high-performance Fe-based catalysts for PS-AOPs.

CRediT authorship contribution statement

Dengke Wang: Conceptualization, Investigation, Data curation, Writing – review & editing, Funding acquisition. **Mengjuan Suo**: Investigation, Formal analysis. **Shiqin Lai and Lanqing Deng**: Investigation, Software, Visualization. **Jiayi Liu, Jun Yang, Siqi Chen and Mei-Feng Wu**: Methodology, Software, Visualization. **Jian-Ping Zou**: Supervision, Conceptualization, Writing – review & editing, Funding acquisition.

Declaration of Competing Interest

The authors declare that they have no known competing financial interests or personal relationships that could have appeared to influence the work reported in this paper.

Data availability

Data will be made available on request.

Acknowledgements

Appendix A. Supporting information

Supplementary data associated with this article can be found in the online version at doi:10.1016/j.apcatb.2022.122054.

References

[1] J. Lee, U. von Gunten, J.H. Kim, Persulfate-based advanced oxidation: critical assessment of opportunities and roadblocks, Environ. Sci. Technol. 54 (2020) 3064–3081.
[2] P.H. Shao, Y.P. Jing, X.G. Duan, H.Y. Lin, L.M. Yang, W. Ren, F. Deng, B.H. Li, X. B. Luo, S.B. Wang, Revisiting the graphitized nanodiamond-mediated activation of peroxymonosulfate: singlet oxygenation versus electron transfer, Environ. Sci. Technol. 55 (2021) 16078–16087.
[3] J.H. Lim, M.R. Hoffmann, Peroxymonosulfate (PMS) activation on cobalt-doped TiO_2 nanotubes: degradation of organics under dark and solar light irradiation conditions, Environ. Sci. Nano 7 (2020) 1602–1611.
[4] J.F. Zheng, W.B. Li, R.D. Tang, S. Xiong, D.X. Gong, Y.C. Deng, Z.P. Zhou, L. Li, L. Su, L.H. Yang, Ultrafast photodegradation of nitenpyram by Ag/Ag_3PO_4/Zn-Al LDH composites activated by persulfate system: removal efficiency, degradation pathway and reaction mechanism, Chemsphere 292 (2022), 133431.
[5] P.C. Xie, L. Zhang, J.H. Chen, J.Q. Ding, Y. Wan, S.L. Wang, Z.P. Wang, A.J. Zhou, J. Ma, Enhanced degradation of organic contaminants by zero-valent iron/sulfite process under simulated sunlight irradiation, Water Res. 149 (2019) 169–178.
[6] X.H. Wang, P. Zhang, C.P. Wang, H.Z. Jia, X.F. Shang, J.C. Tang, H.W. Sun, Metal-rich hyperaccumulator-derived biochar as an efficient persulfate activator: role of intrinsic metals (Fe, Mn and Zn) in regulating characteristics, performance and reaction mechanisms, J. Hazard. Mater. 424 (2022), 127225.
[7] J. Li, L.X. Yang, B. Lai, C. Liu, Y.X. He, G. Yao, N.W. Li, Recent progress on heterogeneous Fe-based materials induced persulfate activation for organics removal, Chem. Eng. J. 414 (2021), 128674.
[8] Z.C. Yang, C. Shan, B.C. Pan, J.J. Pignatello, The Fenton reaction in water assisted by picolinic acid: accelerated iron cycling and co-generation of a selective fe-based oxidant, Environ. Sci. Technol. 55 (2021) 8299–8308.
[9] M.Y. Xing, W.J. Xu, C.C. Dong, Y.C. Bai, J.B. Zeng, Y. Zhou, J.L. Zhang, Y.D. Yin, Metal sulfides as excellent co-catalysts for H_2O_2 decomposition in advanced oxidation processes, Chem 4 (2018) 1359–1372.
[10] L.C. Liu, A. Corma, Confining isolated atoms and clusters in crystalline porous materials for catalysis, Nat. Rev. Mater. 6 (2020) 244–263.
[11] Q. Fu, F. Yang, X.H. Bao, Interface-confined oxide nanostructures for catalytic oxidation reactions, Acc. Chem. Res. 46 (2013) 1692–1701.
[12] J. Ali, L. Wenli, A. Shahzad, J. Ifthikar, G.G. Aregay, I.I. Shahib, Z. Elkhlifi, Z. Chen, Z.Q. Chen, Regulating the redox centers of Fe through the enrichment of Mo moiety for persulfate activation: a new strategy to achieve maximum persulfate utilization efficiency, Water Res. 181 (2020), 115862.
[13] L.S. Zhang, X.H. Jiang, Z.A. Zhong, L. Tian, Q. Sun, Y.T. Cui, X. Lu, J.P. Zou, S. L. Luo, Carbon nitride supported high-loading fe single-atom catalyst for activating of peroxymonosulfate to generate 1o2 with 100% selectivity, Angew. Chem. Int. Ed. 60 (2021) 21751–21755.
[14] J.Y. Chen, Y.K. Kang, W. Zhang, Z.H. Zhang, Y. Chen, Y. Yang, L.L. Duan, Y.F. Li, W. Li, Lattice-confined single-atom Fe_1S_x on mesoporous TiO_2 for boosting ambient electrocatalytic N_2 reduction reaction, Angew. Chem. Int. Ed. (2022), e202203022.
[15] X.H. Zheng, Y.L. Li, Y. Zheng, L.J. Shen, Y.H. Xiao, Y.N. Cao, Y.F. Zhang, C. Au, L. L. Jiang, Highly efficient porous $Fe_xCe_{1-x}O_{2-\delta}$ with three-dimensional hierarchical nanoflower morphology for H2S-selective oxidation, ACS Catal. 10 (2020) 3968–3983.
[16] Q.W. Tang, X.Q. An, H.C. Lan, H.J. Liu, J.H. Qu, Polyoxometalates/TiO_2 photocatalysts with engineered facets for enhanced degradation of bisphenol A through persulfate activation, Appl. Catal. B Environ. 268 (2020), 118394.
[17] J.S. Hu, P.F. Zhang, W.J. An, L. Liu, Y.J. Liang, W.Q. Cui, In-situ Fe-doped g-C_3N_4 heterogeneous catalyst via photocatalysis-Fenton reaction with enriched photocatalytic performance for removal of complex wastewater, Appl. Catal. B Environ. 245 (2019) 130–142.
[18] R.X. Qin, K.L. Liu, Q.Y. Wu, N.F. Zheng, Surface coordination chemistry of atomically dispersed metal catalysts, Chem. Rev. 120 (2020) 11810–11899.
[19] C. Gao, J. Wang, H.X. Xu, Y.J. Xiong, Coordination chemistry in the design of heterogeneous photocatalysts, Chem. Soc. Rev. 46 (2017) 2799–2823.
[20] G.R. Cai, P. Yan, L.L. Zhang, H.C. Zhou, H.L. Jiang, Metal-organic framework-based hierarchically porous materials: synthesis and applications, Chem. Rev. 121 (2021) 12278–12326.
[21] A. Dhakshinamoorthy, Z.H. Li, H. Garcia, Catalysis and photocatalysis by metal organic frameworks, Chem. Soc. Rev. 47 (2018) 8134–8172.
[22] S. Abednatanzi, P.G. Derakhshandeh, H. Depauw, F.-X. Coudert, H. Vrielinck, P. Van Der Voort, K. Leus, Mixed-metal metal–organic frameworks, Chem. Soc. Rev. 48 (2019) 2535–2565.

[23] N. Kolobov, M.G. Goesten, J. Gascon, Metal-organic frameworks: molecules or semiconductors in photocatalysis? Angew. Chem. Int. Ed. 60 (2021) 26038–26052.

[24] A. Mesbah, P. Rabu, R. Sibille, S. Lebègue, T. Mazet, B. Malaman, M. François, From hydrated $Ni_3(OH)_2(C_8H_4O_4)_2(H_2O)_4$ to anhydrous $Ni_2(OH)_2(C_8H_4O_4)$: impact of structural transformations on magnetic properties, Inorg. Chem. 53 (2014) 872–881.

[25] M.B. Stevens, C.D.M. Trang, L.J. Enman, J. Deng, S.W. Boettcher, Reactive Fe-sites in Ni/Fe (oxy)hydroxide are responsible for exceptional oxygen electrocatalysis activity, J. Am. Chem. Soc. 139 (2017) 11361–11364.

[26] D.K. Wang, R.K. Huang, W.J. Liu, D.R. Sun, Z.H. Li, Fe-based MOFs for photocatalytic CO_2 reduction: role of coordination unsaturated sites and dual excitation pathways, ACS Catal. 4 (2014) 4254–4260.

[27] Y.W. Gao, Y. Zhu, T. Li, Z.H. Chen, Q.K. Jiang, Z.Y. Zhao, X.Y. Liang, C. Hu, Unraveling the high-activity origin of single-atom iron catalysts for organic pollutant oxidation via peroxymonosulfate activation, Environ. Sci. Technol. 55 (2021) 8318–8328.

[28] J. Liang, X.G. Duan, X.Y. Xu, K.X. Chen, F. Wu, H. Qiu, C.S. Liu, S.,B. Wang, X. D. Cao, Biomass-derived pyrolytic carbons accelerated Fe(III)/Fe(II) redox cycle for persulfate activation: pyrolysis temperature-depended performance and mechanisms, Appl. Catal. B Environ. 297 (2021) 120446.

[29] G. Kresse, J. Furthmuller, Efficiency of ab-initio total energy calculations for metals and semiconductors using a plane-wave basis set, Comput. Mater. Sci. 6 (1996) 15–50.

[30] J.D. Chen, F. Zheng, S.-J. Zhang, A. Fisher, Y. Zhou, Z.Y. Wang, Y.Y. Li, B.-B. Xu, J.-T. Li, S.-G. Sun, Interfacial interaction between FeOOH and Ni-Fe LDH to modulate the local electronic structure for enhanced OER electrocatalysis, ACS Catal. 8 (2018) 11342–11351.

[31] F.Z. Sun, G. Wang, Y.Q. Ding, C. Wang, B.B. Yuan, Y.Q. Lin, NiFe-based metal-organic framework nanosheets directly supported on nickel foam acting as robust electrodes for electrochemical oxygen evolution reaction, Adv. Energy Mater. 8 (2018), 1800584.

[32] C.-F. Li, L.-J. Xie, J.-W. Zhao, L.-F. Gu, H.-B. Tang, L.R. Zheng, G.-R. Li, Interfacial Fe-O-Ni-O-Fe bonding regulates the active Ni sites of Ni-MOFs via iron doping and decorating with FeOOH for super-efficient oxygen evolution, Angew. Chem. Int. Ed. 61 (2022), e202116934.

[33] J.Y. Chen, P.Y. Zhuang, Y.C. Ge, H. Chu, L.Y. Yao, Y.D. Cao, Z.Y. Wang, M.O. L. Chee, P. Dong, J.F. Shen, M.X. Ye, P.M. Ajayan, Sublimation-vapor phase pseudomorphic transformation of template-directed MOFs for efficient oxygen evolution reaction, Adv. Funct. Mater. 29 (2019), 1903875.

[34] Y.M. Wang, P. Zhang, T. Li, L. Lyu, Y.W. Gao, C. Hu, Enhanced Fenton-like efficiency by the synergistic effect of oxygen vacancies and organics adsorption on Fe_xO_y-d-g-C_3N_4 with Fe–N complexation, J. Hazard. Mater. 408 (2021), 124818.

[35] V. Rubio-Giménez, J.C. Waerenborgh, J.M. Clemente-Juan, C. Martí-Gastaldo, Spontaneous magnetization in heterometallic NiFe-MOF-74 microporous magnets by controlled iron doping, Chem. Mater. 29 (2017) 6181–6185.

[36] J.Y.C. Chen, L. Dang, H.F. Liang, W.L. Bi, J.B. Gerken, S. Jin, E.E. Alp, S.S. Stahl, Operando analysis of NiFe- and Fe-oxyhydroxide electrocatalysts for water oxidation: detection of Fe^{+4} by Mössbauer spectroscopy, J. Am. Chem. Soc. 137 (2015) 15090–15093.

[37] Y. Yue, C.C. Shen, Y. Ge, Biochar accelerates the removal of tetracyclines and their intermediates by altering soil properties, J. Hazard. Mater. 380 (2019), 120821.

[38] P.H. Shao, J.Y. Tian, F. Yang, X.G. Duan, S.S. Gao, W.X. Shi, X.B. Luo, F.Y. Cui, S. L. Luo, S.B. Wang, Identification and regulation of active sites on nanodiamonds: establishing a highly efficient catalytic system for oxidation of organic contaminants, Adv. Funct. Mater. 28 (2018), 1705295.

[39] Y.G. Bu, H.C. Li, W.J. Yu, Y.F. Pan, L.J. Li, Y.F. Wang, L.T. Pu, J. Ding, G.D. Gao, B. C. Pan, Peroxydisulfate activation and singlet oxygen generation by oxygen vacancy for degradation of contaminants, Environ. Sci. Technol. 55 (2021) 2110–2120.

[40] M.J. Huang, Y. Han, W. Xiang, D.L. Zhong, C. Wang, T. Zhou, X.H. Wu, J. Mao, In situ-formed phenoxyl radical on the CuO surface triggers efficient persulfate activation for phenol degradation, Environ. Sci. Technol. 55 (2021) 15361–15370.

[41] Y.D. Xue, N.N.T. Pham, G. Nam, J. Choi, Y.-Y. Ahn, H. Lee, J. Jung, S.-G. Lee, J. Lee, Persulfate activation by ZIF-67-derived cobalt/nitrogen-doped carbon composites: kinetics and mechanisms dependent on persulfate precursor, Chem. Eng. J. 408 (2021), 127305.

[42] J.H. Qu, Y. Xu, X.B. Zhang, M.Z. Sun, Y. Tao, X.M. Zhang, G.S. Zhang, C.J. Ge, Y. Zhang, Ball milling-assisted preparation of N-doped biochar loaded with ferrous sulfide as persulfate activator for phenol degradation: multiple active sites-triggered radical/non-radical mechanism, Appl. Catal. B Environ. 316 (2022), 121639.

[43] P. Huang, P. Zhang, C.P. Wang, J.C. Tang, H.W. Sun, Enhancement of persulfate activation by Fe-biochar composites: synergism of Fe and N-doped biochar, Appl. Catal. B Environ. 303 (2022), 120926.

[44] M.J. Pu, J.F. Niu, M.L. Brusseau, Y.L. Sun, C.Z. Zhou, S. Deng, J.Q. Wan, Ferrous metal-organic frameworks with strong electron-donating properties for persulfate activation to effectively degrade aqueous sulfamethoxazole, Chem. Eng. J. 394 (2020), 125044.

[45] Y.W. Wu, X.T. Chen, Y. Han, D.T. Yue, X.D. Cao, Y.X. Zhao, X.F. Qian, Highly efficient utilization of nano-Fe(0) embedded in mesoporous carbon for activation of peroxydisulfate, Environ. Sci. Technol. 53 (2019) 9081–9090.

[46] H.X. Zhang, L.-C. Nengzi, Z.J. Wang, X.Y. Zhang, B. Li, X.W. Cheng, Construction of Bi_2O_3/CuNiFe LDHs composite and its enhanced photocatalytic degradation of lomefloxacin with persulfate under simulated sunlight, J. Hazard. Mater. 383 (2020), 121236.

[47] D.K. Wang, H. Zeng, S.Q. Chen, L. Tian, D.M. Hou, Y. Mu, S.L. Wu, J.-P. Zou, Selective regulation of peroxydisulfate-to-hydroxyl radical for efficient in-situ chemical oxidation over Fe-based metal-organic frameworks under visible light, J. Catal. 406 (2022) 1–8.

[48] W.-Q. Li, Y.-X. Wang, J.-Q. Chen, N.N. Hou, Y.M. Li, X.C. Liu, R.R. Ding, G.N. Zhou, Q. Li, X.G. Zhou, Y. Mu, Boosting photo-Fenton process enabled by ligandto-cluster charge transfer excitations in iron-based metal organic framework, Appl. Catal. B Environ. 302 (2022), 120882.

[49] M.H. Li, S.J. You, X.G. Duan, Y.B. Liu, Selective formation of reactive oxygen species in peroxymonosulfate activation by metal-organic framework-derived membranes: a defect engineering-dependent study, Appl. Catal. B Environ. 312 (2022), 121419.

[50] T. Wang, J.J. Zhou, W.J. Wang, Y.Q. Zhu, J.F. Niu, Ag-single atoms modified $S_{1.66}$-$N_{1.91}$/TiO_{2-x} for photocatalytic activation of peroxymonosulfate for bisphenol A degradation, Chin. Chem. Lett. 33 (2022) 2121–2124.

[51] M. Zhu, L. Zhang, S. Liu, D. Wang, Y. Qin, Y. Chen, W. Dai, Y. Wang, Q. Xing, J. Zou, Degradation of 4-nitrophenol by electrocatalysis and advanced oxidation processes using Co_3O_4@C anode coupled with simultaneous CO_2 reduction via SnO_2/CC cathode, Chin. Chem. Lett. 31 (2020) 1961–1965.

[52] Z. Wang, W. Qiu, S.Y. Pang, Y. Gao, Y. Zhou, Y. Cao, J. Jiang, Relative contribution of ferryl ion species (Fe(IV)) and sulfate radical formed in nanoscale zero valent iron activated peroxydisulfate and peroxymonosulfate processes, Water Res. 172 (2020), 115504.

[53] C.J. Liang, H.W. Su, Identification of sulfate and hydroxyl radicals in thermally activated persulfate, Ind. Eng. Chem. Res. 48 (2009) 5558–5562.

[54] Y. Zhao, H.Z. An, J. Feng, Y.M. Ren, J. Ma, Impact of crystal types of $AgFeO_2$ nanoparticles on the peroxymonosulfate activation in the water, Environ. Sci. Technol. 53 (2019) 4500–4510.

[55] Z.-Y. Zhao, X.X. Sun, H.W. Gu, Z. Niu, P. Braunstein, J.-P. Lang, Engineering the electronic structures of metal-organic framework nanosheets via synergistic doping of metal ions and counteranions for efficient water oxidation, ACS Appl. Mater. Interfaces 14 (2022) 15133–15140.

[56] P.M. Kouotou, M. Waqas, A.E. Kasmi, Z. Atour, Z.-Y. Tian, Influence of Co addition on Ni-Co mixed oxide catalysts toward the deep oxidation of low-rank unsaturated hydrocarbons, Appl. Catal. A Gen. 612 (2021), 117990.